Bio-Design and Manufacturing (2026) 9:563–578
https://doi.org/10.1631/bdm.2600041

RESEARCH ARTICLE

Minimalistic metabolite piezoelectric self-assembly for the development of implantable bioelectronics for in vivo monitoring

Zengfeng Qiu[1,2,4] · Ruiqi Liu[2,3,4] · Haoye Jiang[2,3,4] · Xiaoyue Ma[1,4] · Lujing Gao[1,2,4] · Zixuan Liu[2,4] · Jiahao Zhang[4,5] · Yancheng Wang[3,4] · Jiqian Wang[1,4] · Syed A. M. Tofail[4,6] · Deqing Mei[3,4] · Hai Xu[1,3] · Kai Tao[2,3,4]

Received: 19 January 2026 / Accepted: 4 March 2026 / Published online: 28 April 2026

Abstract

Amino acid non-centrosymmetric self-assemblies, possessing inherent polarization as well as biocompatibility, can be employed as bioinspired alternatives for the development of implantable piezoelectric bioelectronics. This could enable the harvesting of biomechanical energy for in situ in vivo monitoring and avoid the need for secondary surgeries, potentially overcoming the trade-off between high-efficiency sensing and the biosafety limitations of traditional inorganic or polymeric piezoelectric counterparts. In this regard, the electromechanical coupling behaviors of the minimalistic metabolite self-assemblies are reported. Experimental tests reveal that compared to other natural amino acid crystals, threonine (T) crystals exhibit a high Young's modulus of up to approximately 80 GPa by forming a denser three-dimensional hydrogen-bonding network, with each molecule interacting with seven adjacent ones. Computational analysis reveals that side-chain entities dramatically affect crystal packing, with polar hydroxyl moieties accounting for the distinct piezoelectric features underlying the macroscopic performance. This highlights the potential of exploiting T crystals to develop biodegradable piezoelectric bioelectronics that exhibit highly sensitive linear responses for tactile sensing and post-implantation in vivo motion monitoring. This study demonstrates the feasibility of exploiting minimalistic metabolite self-assemblies for piezoelectric bioelectronics in bio-machine interface and biomedical engineering applications.

✉ Hai Xu
xuh@upc.edu.cn

✉ Kai Tao
kai.tao@zju.edu.cn

[1] College of Chemistry and Chemical Engineering, China University of Petroleum (East China), Qingdao 266580, China

[2] Zhejiang-Israel Joint Laboratory of Self-Assembled Functional Materials, ZJU-Hangzhou Global Scientific and Technological Innovation Center, Hangzhou 311215, China

[3] State Key Laboratory of Fluid Power and Mechatronic Systems, Zhejiang Key Laboratory of Advanced Equipment Manufacturing and Measurement Technology, School of Mechanical Engineering, Zhejiang University, Hangzhou 310058, China

[4] Zhejiang-Ireland Joint Laboratory of Bio-organic Dielectric Materials & Devices, Hangzhou 310058, China

[5] School of Mechanical Engineering, Zhejiang Sci-Tech University, Hangzhou 310018, China

[6] Department of Physics and Bernal Institute, University of Limerick, Limerick V94 T9PX, Ireland

Graphical abstract

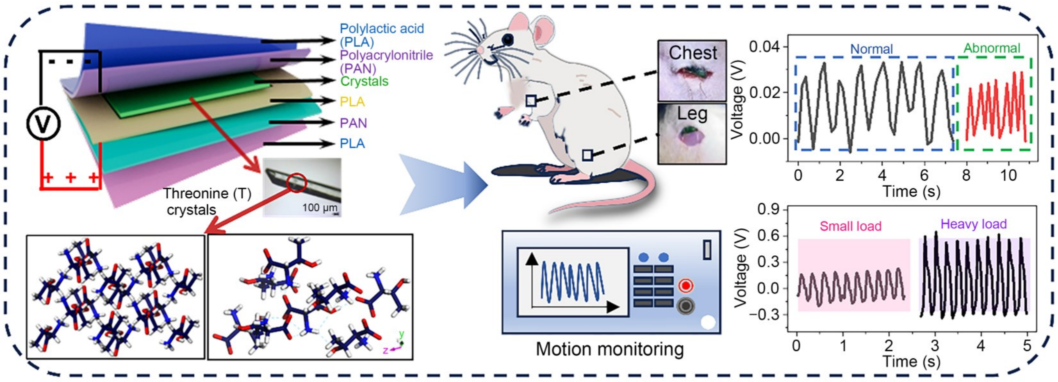

Keywords Metabolites · Piezoelectricity · Implantable bioelectronics · Self-assembly

1 Introduction

The development of novel piezoelectric systems for diagnostic and therapeutic monitoring has attracted significant research attention, driven by the growing demand for flexible adaptation, histocompatibility, and environmental compatibility for bioelectronic devices [1–7]. Although inorganic ceramics (e.g., barium titanate (BTO) [8]) and organic polymers (e.g., polyvinylidene difluoride (PVDF) [9–11]) exhibit excellent electromechanical conversion properties, their inherent biotoxicity and metabolic residue issues severely limit their expansion in applications for implantable medical devices. In this context, crystalline materials based on amino acid molecules are regarded as ideal candidate systems for next-generation bio-piezoelectric materials due to their natural biosafety, affinity properties, degradability, and green-scale synthesis. In particular, using crystal materials with various side-chain properties and tyrosine (Y) [12, 13], threonine (T), and other basic amino acids [14] as building blocks not only provides a unique platform for asymmetric modulation of crystals due to their diverse molecular conformations, but also retains the intrinsic physicochemical properties of natural amino acids. These amino acid crystalline materials are particularly suitable for the development of in vivo degradable physiological signal-sensing systems and offer unique advantages for long-term implantation and monitoring scenarios that require a balance between material safety and environmental friendliness.

Molecular piezoelectric crystals have attracted attention for their immense potential in solid-state piezoelectricity [15, 16]. Recent breakthroughs, such as flexible ferroelectric/piezoelectric crystals [15] and the discovery of the self-healing properties of piezoelectric crystals [17], have significantly advanced this field. A series of studies has provided in-depth explorations of the piezoelectric properties of molecular crystals, such as amino acids, using computational and experimental approaches, revealing the high piezoelectric response of β- and γ-glycine [18–20]. These advancements highlight the potential of organic materials to replace traditional inorganic piezoelectric ceramics. However, despite the ongoing research boom, a significant gap persists between the fundamental design principles of molecular crystal microstructures and their macroscopic piezoelectric properties. The intrinsic relationship between structure and performance in such materials remains unclear, hindering the design of high-performance piezoelectric biomaterials. The present study analyzed structural features, such as molecular side chains, and quantitatively correlated intermolecular interactions, crystal mechanics, and piezoelectric response to guide future material development.

The study focuses on four common natural amino acids categorized by their side-chain structure: the hydrophobic aromatic amino acids phenylalanine (F) and Y, and the hydroxyl group-containing hydrophilic amino acids serine (S) and T. Two categories of molecules represent different forms of intermolecular forces, namely π–π stacking and hydrogen bonding. The hydroxyl groups, replacing the hydrogen atom in the F/Y category and located at different positions in the S/T category, affect steric repulsion and, consequently, molecular packing in crystalline structures. Such interactions, which affect the balance with other forces, such as hydrophobic forces and dipole−dipole interactions, enrich the possible self-assembly and packing patterns. Furthermore, these amino acid building blocks, which are present in physiological environments, ensure biosafety and biodegradability for potential applications. We characterized the molecular stacking structure, mechanical properties of the crystals, and self-assembled morphology using scanning electron microscopy (SEM), single-crystal X-ray diffraction (SC-XRD), and atomic force microscopy (AFM) (Scheme 1), demonstrating that the crystalline structures were influenced by both growth conditions and molecular structure.

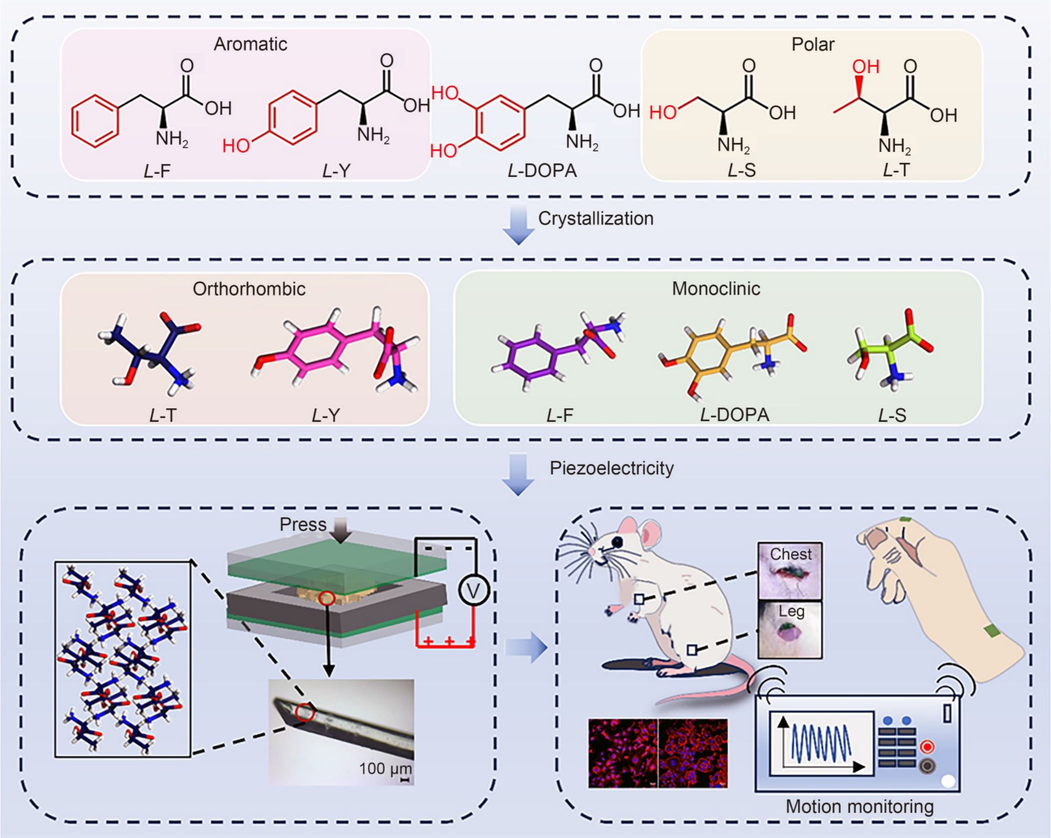

Scheme 1 Schematic presentation of natural amino acids with different side chains self-assembled into diverse non-centrosymmetric crystals, which can be employed to develop piezoelectric bioelectronics for sensing at the bio-machine interface and for in vivo monitoring

Notably, density functional theory (DFT) calculations combined with experimental analyses revealed that the crystals exhibit surprisingly good mechanical properties, with Young's modulus up to approximately 80 GPa. More importantly, we successfully fabricated biocompatible piezoelectric sensors from the aforementioned amino acid crystals that exhibit piezoelectric properties. The fabricated sensors enable real-time in vivo monitoring of dynamic physiological signals. Our research reveals the effect of intermolecular hydrogen bonding on macroscopic piezoelectric properties and offers new possibilities for the biocompatible fabrication of soft implants.

2 Materials and methods

2.1 Materials

All chemicals used in this study were commercially available and used directly without further purification. *L*-F, *L*-Y, *L*-S, and *L*-T powder and *L*-3,4-dihydroxyphenylalanine (*L*-DOPA) were procured from Sigma-Aldrich (Merck KGaA, Darmstadt, Germany; purity ⩾98%). Water was treated using a purification system (Millipore Ellix, Milli-Q Biocel, Germany) with resistivity above 18.2 MΩ·cm.

2.2 Crystal preparation

Amino acids F, Y, DOPA, S, and T were individually dissolved in water at concentrations of 200 mmol/L, 10 mmol/L, 70 mmol/L, 4 mol/L, and 2 mol/L at 80 °C, respectively. Then, they were filtered through a 0.45 μm membrane at the same temperature. Crystals formed when the solution was cooled to room temperature and were collected after 7 d of incubation (Fig. S1 in the supplementary information).

2.3 Scanning electron microscopy

The crystal dispersion was dropped onto a clean silicon wafer and adsorbed for 30 s. Excess solution was then removed. The sample was then kept at 40 °C for 8 h. Prior to imaging, a 10-nm-thick gold layer was deposited on the samples. The surface morphology of the crystals was captured using a field-emission scanning electron microscope (JSM-7900F, JEOL, Japan) at an accelerating voltage of 5 kV.

2.4 Powder X-ray diffraction (XRD)

The XRD patterns of all crystals were acquired using an X-ray powder diffractometer (X'Pert Pro MPD, Panalytical, the Netherlands) at room temperature. The 2θ range was set between 5° and 80°, with a scan rate of 5 (°)/min and a step size of 0.02°.

2.5 Single-crystal X-ray diffraction

Crystallographic characterization was carried out on a single-crystal diffractometer (SuperNova E, Agilent Technologies, Inc., Santa Clara, CA, USA) with a micro-focal spot copper target (Cu-Kα, λ=1.541 84 Å; 1 Å=1×10^{-10} m). Commercially available software packages CrysAlisPro, Olex2, and Superflip were used to analyze the collected data, and the structure was refined using the SHELXL software package for full-matrix least squares.

2.6 Theoretical calculations

All DFT computations were conducted using the Vienna Ab-initio Simulation Package (VASP) [21, 22]. The electronic exchange−correlation interactions were approximated using the generalized gradient approximation (GGA) with the Perdew−Burke−Ernzerhof (PBE) functional [23]. To model core–electron interactions, the projected augmented wave (PAW) method [24, 25] was implemented, while valence electrons were represented by a plane-wave basis set with a kinetic energy cutoff of 450 eV to ensure computational accuracy.

The Kohn–Sham orbital occupancies were treated using Gaussian smearing with a width parameter of 0.05 eV to mitigate convergence challenges near the Fermi level. For Brillouin zone sampling during structural optimization (including both atomic coordinates and lattice parameters), a Γ-centered k-point grid with a spacing of 0.04 Å^{-1} was systematically generated [26]. Self-consistent field (SCF) iterations were terminated when the total energy difference between consecutive steps fell below 10^{-8} eV, ensuring high-precision electronic convergence. Geometries were optimized until the residual forces on all atoms were reduced to less than 0.001 eV/Å, guaranteeing stable equilibrium configurations.

To accurately account for van der Waals interactions essential in weakly bonded systems, the semi-empirical DFT-D3 dispersion correction scheme proposed by Grimme et al. [27, 28] was employed. Spin-polarized calculations were explicitly performed to address magnetic interactions in the investigated systems. Elastic tensor analyses, including Young’s modulus determination, were executed via the elastic anisotropy measures (ElAM) [29] and ELATE [30] post-processing modules, which derive mechanical properties from second-order derivatives of the energy−strain relationship. Rigorous validation of mechanical stability was performed by verifying compliance with Born−Huang criteria for all optimized crystal structures.

2.7 Young’s modulus measurement

Mechanical properties were measured at the nanoscale using an atomic force microscope (MultiMode 8, Bruker, USA) with a NanoScope V controller (Bruker) in air. A single-crystal silicon probe (RTESPA-525, Bruker; cantilever length, width, and thickness of 125, 40, and 5.75 μm, respectively; tip radius of curvature of 8 nm; flexural resonant frequency of 525 kHz; spring factor of 200 N/m) was used in the experiments. Briefly, crystals were adsorbed on a clean silicon substrate, and the cantilever was moved above the crystals under an optical microscope. The tip approaches the crystal surface at a constant velocity, generating a linear force curve with respect to time. The Young’s modulus was estimated by fitting the force–distance curve to the Hertzian model. Based on the mechanical contact model, the probe contact force (F) as a function of indentation depth (h) can be expressed as follows:

$$F(h) = \frac{2}{\pi} \tan\alpha \, \frac{E}{1-v^2} h^2, \tag{1}$$

where α is the half-cone angle of the probe, E is the modulus of elasticity of the crystals, and v is Poisson’s ratio, which is selected as 0.5. Typically, three or five regions (5 μm×5 μm) were randomly selected for each sample for statistical analysis.

2.8 Point stiffness measurement

In the AFM nanoindentation test, the physical nature of the measured point stiffness (k_{meas}) is the equivalent stiffness of the cantilever beam-sample composite system, which comprises the intrinsic stiffness of the cantilever (k_{can}) and the local stiffness constant (k_{cry}) of the crystal. Based on the principle of superposition of elastomers in series, the point stiffness of the crystal can be calculated by Eq. (2):

$$k_{\text{cry}} = \frac{k_{\text{can}} \times k_{\text{meas}}}{k_{\text{can}} - k_{\text{meas}}}. \tag{2}$$

2.9 Piezoresponse force microscopy (PFM)

The piezoelectric coefficient d_{33} of the crystal was measured using an AFM (MultiMode 8, Bruker) in a contact PFM mode. The deflection sensitivity of the probe (SCM-PIT-V2, Bruker; with a spring factor of 3 N/m) was calibrated using a sapphire specimen. When the tip is in contact with the sample, a 5-V alternating current (AC) voltage is applied to the AFM probe, and a piezoelectric response is generated. The phase and amplitude signals of the tip were recorded to determine the piezoelectric constant. To determine d_{33}, the vertical piezoelectric response was recorded under an applied AC voltage of 1–10 V. The data were analyzed using NanoScope Analysis software (Bruker), and d_{33}

was extracted from the slope of the amplitude–voltage curve. Three regions were recorded for each sample for statistical analysis.

2.10 Quasi-static d_{33} measurements of the crystal

Quasi-static d_{33} measurements normal to the crystal films were performed using a piezometer (ZJ-4AN, IACAS, China) under a dynamic force of 0.36 N.

2.11 Fabrication of flexible sensors

The polylactic acid (PLA) substrate film was first prepared by dissolving PLA in dichloromethane (DCM) to obtain a 50 mg/mL solution. The solution was cast onto a flat glass dish and evaporated at 25 °C overnight, yielding a homogeneous PLA film of uniform thickness. Then the PLA-polyacrylonitrile (PAN) electrodes were prepared, and the prepared PLA membrane was cut into 10 mm×10 mm squares, sonicated in 0.5 mol/L sulfuric acid for 20 min, and then rinsed with water and dried in ambient air. Next, a single side of the cleaned PLA membrane was immersed in a mixed solution of 1 mol/L hydrochloric acid and 0.3 mol/L aniline at 0 °C for 2 h to promote aniline polymerization. After the reaction was completed, the residual solution on the surface was fully rinsed with deionized water and dried at room temperature for 12 h. The PLA-PAN conductive electrode was produced with a thickness of about 140 µm. To encapsulate the flexible sensor, the intermediate layer of PLA film is drilled with a central hole (length: 5 mm; width: 5 mm; thickness: 0.7 mm), which is then filled with tightly packed crystals. The crystal layer was placed between two PLA-PAN electrodes, forming an electrode–crystal–electrode sandwich structure, and the through-hole region served as the core sensitive area of the flexible sensor. The layers were glued using 50 mg/mL PLA in DCM to ensure the proper seal of the fabricated sensor. The overall thickness of the flexible sensor was approximately 1 mm.

2.12 In vitro and in vivo testing of flexible sensors

Polyimide-enamelled copper wires (0.2 mm diameter) were connected to the PAN conductive layer to transmit the piezoelectric signals. External forces were applied to the sensors via a linear motor (QDA60, Zolix, China), and an output signal was captured using a high-resistance electrometer (Keithley 6517B, Keithley Instruments, USA). For in vitro testing, the flexible sensors were attached to the surfaces of a volunteer's fingers and wrists, and the body motion signal was collected. For in vivo testing, fabricated sensors were implanted underneath the skin of the chest or left thigh of 8-week-old male Sprague–Dawley rats (body weight (290±10) g, *N*=3). A 15-mm skin incision was made in the shaved area, a flexible sensor was implanted, and two copper wires were led out of the body. The external wires were connected to a computerized recorder (BL-420S BioMachine Experimental System, Chengdu Taimeng, China) to collect signal outputs from chest motion during voluntary respiration and thigh movement.

2.13 In vivo biocompatibility evaluation of flexible sensors

To assess cytotoxicity, MDA-MB-231 human breast cancer cells were selected as a model system, and cells were inoculated into confocal dishes at 6×10^4 cells/dish in the presence of a flexible sensor and cultured overnight in a CO_2-free, 37 °C thermostat incubator to allow the cells to adhere to the wall. Staining was performed using the calcein acetoxymethyl ester/propidium iodide (Calcein-AM/PI) kit. The staining was terminated by washing three times using phosphate-buffered saline (PBS), and the results were observed and photographed.

Fluorescence images were captured using a laser confocal microscope (LSM 900, Carl Zeiss Group, Germany). Cells in confocal dishes were washed three times with PBS to remove excess medium, and 4% paraformaldehyde was added to fix the cells for 10 min. Cells were washed once with PBS and then permeabilized with 0.5% Triton X-100 for 10 min at room temperature. Cells were washed once with PBS, and 4',6-diamidino-2-phenylindole (DAPI) staining solution was added. The working solution was incubated for 30 min at room temperature. Then, fluorescein isothiocyanate (FITC)-labeled phalloidin working solution was added and incubated for 30 min at room temperature. For cytomorphological analysis, the cytoskeleton and nucleus were stained with phalloidin and DAPI, respectively. Images were acquired after 24 and 48 h using confocal microscopy.

3 Results and discussion

3.1 Crystallographic analysis

To systematically investigate the effect of side-chain chemistry on crystal packing [31] and the resulting properties, a series of natural *L*-amino acids was selected. The study focused on T, which possesses a hydroxyl group, and compared it with S, another hydrophilic amino acid with a hydroxyl group, and with F and Y, which contain aromatic benzene rings. DOPA was also included as a more complex aromatic analogue. The morphology of the prepared single crystals (Fig. S1 in the supplementary information) varied significantly with the amino acid side chain. SEM revealed that T crystals exhibit a rod-like shape, whereas F and Y crystals are needle-like, S crystals are plate-like, and DOPA crystals are blocky (Fig. S2 in the supplementary information). The powder XRD (PXRD) results indicate a high average crystallinity, suitable for single crystal analysis (Fig. S3 in the supplementary information).

The single-crystal structure of T, solved by SC-XRD, reveals an orthorhombic system with the non-centrosymmetric space group $P2_12_12_1$ (Table S1 in the supplementary information). The asymmetric packing unit [32, 33] contains one T molecule (Fig. 1a), and the unit cell comprises four molecules (Fig. 1b). The stability of the T crystal is primarily derived from an extensive three-dimensional (3D) hydrogen-bonding network. Each molecule interacts with seven neighboring molecules through hydrogen bonds (Fig. 1c). The amphiphilic nature of the T molecule is a defining feature, leading to a unique zip-like interlocking structure formed via classic electrostatic interactions [34, 35] between the positively charged NH_3^+ and negatively charged COO^- groups. Furthermore, the hydroxyl (OH) group on the β-carbon (C_β) and the hydrogen on the α-carbon (C_α) participate in the hydrogen-bonding network. The C_α hydrogen bonds with the hydroxyl oxygen of an adjacent molecule, while the OH group donates a hydrogen bond to the carboxyl oxygen of another molecule ($d(O_{hydroxyl}\cdots O_{carboxyl})=1.9$ Å, $d(N_{amino}\cdots O_{carboxyl})=1.9$ Å) [36] (Fig. 1d). This intricate network, modulated by both hydrogen bonding and C_α–H interactions, governs the molecular stacking, with the hydrogen bonding controlling the combination primarily on the C_α–H branches and enhancing the packing density.

In contrast, although they share some elemental similarities, the other amino acids exhibit distinct crystal structures. S, which also possesses a hydroxyl group, crystallizes in the monoclinic space group P_n. Its unit cell contains four S molecules (Figs. S4a and S4b in the supplementary information). In the S crystal, each molecule interacts with six neighbors (Fig. S4c in the supplementary information). The packing is characterized by a layered arrangement along the *b*–*c* crystallographic plane (Fig. S4d in the supplementary information), with intermolecular hydrogen bonding between layers providing stability. Although both T and S contain hydroxyl groups, the marked difference in their stacking patterns stems from a crucial stereochemical distinction. An additional methyl group attached to T's C_β introduces significant steric hindrance. This bulky methyl group prevents molecular sliding, thereby inhibiting the formation of the simple layered arrangement observed in S crystals. To simultaneously accommodate the hydrogen-bonding interactions of hydrophilic groups (hydroxyl, amino, and carboxyl) and the stacking requirements of hydrophobic methyl groups, T molecules are compelled to form a more complex, spatially highly interlocked 3D network. It is precisely this steric-driven stacking mechanism that results in its higher packing density, thereby conferring mechanical rigidity far exceeding that of S crystals.

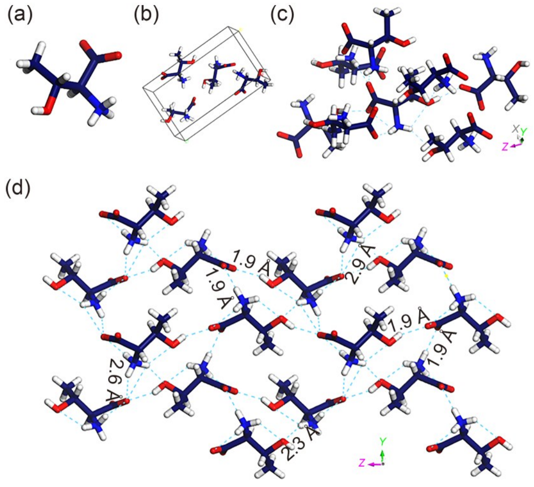

Fig. 1 Crystallographic structure of T crystals. (a) Asymmetric unit. (b) The crystalline cell. (c) Intermolecular hydrogen-bonding network. (d) Analysis of intermolecular interactions. The carbon, nitrogen, hydrogen, and oxygen atoms are colored dark blue, blue, white, and red, respectively. 1 Å=1×10^{-10} m

The aromatic amino acids F and Y introduce different intermolecular forces. Y crystallizes in the same orthorhombic system ($P2_12_12_1$) as T, whereas F belongs to the monoclinic $P2_1$ space group. F's crystal cell contains eight molecules [37, 38] (Figs. S5a and S5b in the supplementary information). Direct hydrogen bonding connects each molecule to four neighbors (Fig. S5c in the supplementary information), and the benzene rings play a key role in forming antiparallel dimers, which serve as basic building blocks arranged in layers (Fig. S5d in the supplementary information). The stability of F and Y crystals is significantly influenced by C–H···π interactions (Figs. S6–S8 in the supplementary information). In Y, two molecules form a planar rhombic dimer, and neighboring dimers are further connected by a network of hydrogen bonds to form an antiparallel supramolecular β-sheet structure [12, 13] (Fig. S7 in the supplementary information). Contrasting with the hydrogen-bond-dominated structure of T, the packing in F and Y represents a delicate balance of hydrogen bonds and weaker C–H···π interactions, resulting in distinct structural and mechanical properties.

Conversely, DOPA behaves significantly differently from F and Y. Its structure involves one molecule in the asymmetric unit, and the small unit cell contains only two molecules (Figs. S9a and S9b in the supplementary information). Each DOPA molecule forms direct hydrogen bonds with six neighboring molecules, arranged along the crystallographic *b*-direction to form an interlocked structure (Figs. S9c and S9d in the supplementary information). Here, π–π stacking interactions are perturbed, and C–H···π interactions become the primary stabilizing force (Fig. S10 in the supplementary information). This reliance on non-covalent interactions provides a structural basis for the rational design of stacking modes in aromatic amino acid biomaterials.

The crystal structures of different amino acids exhibit pronounced side-chain-dependent variations (e.g., polarity, volume, and distribution of hydrophilic groups). These structural differences modulate the orientation and strength of intermolecular force networks (such as hydrogen bonds and C–H···π interactions), thereby determining supramolecular assembly patterns and crystal stacking. While hydrogen-bonding networks confer stability, they also predetermine the mechanical flexibility of the crystal. More importantly, these side-chain-dominated stacking patterns directly influence geometric parameters such as bond lengths and angles [31, 39], ultimately determining whether the crystal exhibits non-centrosymmetric structures, which is a prerequisite for generating piezoelectric effects. Consequently, side-chain architecture is likely the fundamental cause of macroscopic variations in piezoelectric properties.

3.2 Mechanical characterizations

The engineering application of molecular crystals is highly dependent on the synergistic optimization of performance parameters, including controllable availability, low-defect crystal growth, thermochemical stability, and mechanical response properties, which together form the cornerstone of material functionalization. For endogenous biomaterials such as amino acid crystals, their mechanical properties (e.g., resistance to brittle cracking) directly determine their longevity and reliability in real-world applications such as drug carriers and biosensors. Central to this research is the elastic constant tensor, which not only quantitatively characterizes the anisotropic response of crystals to external mechanical stresses (e.g., spatial distribution of Young's modulus), but also builds a computable physicochemical model for the analysis of the "structure–property" relationship by correlating the intermolecular forces with the macroscopic mechanical behaviors across scales. The primary objective of the current study is to reveal how the dynamic rearrangement of amphiphilic groups in amino acid crystals can facilitate mechanical flexibility by reconstructing hydrogen-bonding topologies, thereby breaking the brittleness bottleneck in traditional molecular crystals. By combining experiments, first-principles calculations, and theoretical work, we aim to elucidate the crystal stacking characteristics and their intrinsic relationship with mechanical properties, particularly the anisotropic spatial distribution features characterized by the elasticity tensor [40–42].

The crystal packing mode directly determines mechanical properties, and mechanical stability is a prerequisite for sensors to achieve long-term monitoring within the complex mechanical environment of the body. Based on the SC-XRD results, the side-chain structure directly governs crystal packing and macroscopic performance by modulating the type and density of non-covalent interactions: T forms a 3D hydrogen-bonding network involving both its C_β hydroxyl and C_α hydrogen, with the dense crosslinking of hydrogen bonds significantly increasing packing density. In contrast, although S also contains a hydroxyl group, differences in its side-chain structure lead to a layered packing mode, resulting in weaker hydrogen bond continuity.

Aromatic amino acids (F and Y) rely on a synergistic balance between hydrogen bonds, π–π stacking, and C–H···π interactions, leading to less dense packing. This difference in packing is directly reflected in the mechanical properties: the Young's modulus of T crystals measured using AFM reaches (83.7±0.5) GPa, significantly higher than that of F ((10.4±0.1) GPa), S ((35.3±0.1) GPa), and Y ((41.3±0.4) GPa), confirming that the density of the hydrogen-bonding network is key to enhancing crystal rigidity (Figs. S11 and S12 in the supplementary information). Meanwhile, the point stiffness trend of the crystals is consistent with the Young's modulus (Fig. S13 in the supplementary information), and is also seen in the nanoindentation measurement (Fig. S14 in the supplementary information), where T crystals exhibit the largest Young's modulus among all samples. However, the absolute values of Young's modulus measured by nanoindentation were generally lower than those obtained via AFM.

The discrepancy in the values obtained from the two testing techniques stems from the crystal's structural heterogeneity. In PeakForce mode, AFM probes the surface of the crystal. This region, influenced by growth conditions, exhibits a more complete hydrogen-bond network and fewer defects, resulting in a measured Young's modulus that closely approximates the theoretical value for a perfect crystal. In contrast, nanoindentation involves greater penetration depth, probing the bulk phase of the crystal. Minor growth defects in the bulk, such as interlayer voids or microcracks, can reduce overall rigidity, leading to lower measured values. This discrepancy indirectly confirms that the high modulus of T crystals arises from a hydrogen-bonding network-dominated structure that extends from the surface to the bulk, and that defects in the bulk phase have a limited impact on mechanical performance. This finding further supports the structural stability of T crystals as a core material for sensors. Furthermore, the Young's modulus values of the amphipathic amino acid crystals were significantly higher than those of N-acetylated counterparts, such as L-AcN [31], indicating the effect of hydrogen-bonding interactions. This variation with contact position is a direct manifestation of the crystal's anisotropy. Although the crystals predominantly lie with their main facet parallel to the substrate, the

AFM probe interacts with local surface topography, such as atomic steps or minor defects. This effectively probes the mechanical response along slightly different orientations, causing fluctuations in the measured values within the theoretically predicted range between the maximum ($E_{\max}$, rose lines in Figs. 2e–2h) and minimum ($E_{\min}$, green lines in Figs. 2e–2h) Young's moduli.

To understand the structural origins of these mechanical properties, the elastic behavior was computationally investigated using DFT simulations (Table 1; Table S2 in the supplementary information). These calculations revealed a strong anisotropy in the Young's modulus for all investigated crystals. The magnitude of the modulus was found to be highly dependent on the loading direction relative to the crystal's internal structure (Fig. 2; Fig. S15 in the supplementary information). Specifically, high Young's moduli (up to 70–90 GPa) [43, 44] were predicted when external compression was applied perpendicular to the average orientation of dense hydrogen-bond networks. This orientation dependence arises because denser molecular packing, induced by the hydrogen-bond network, offers greater resistance to deformation, leading to a higher measured modulus. Conversely, directions with weaker intermolecular interactions or larger voids exhibit lower stiffness.

The T-crystal, in particular, displayed the highest degree of elastic anisotropy, being 1–2 times more anisotropic than the other samples, especially along the *z*-axis (001 face) [40, 44] (Figs. 2d and 2h). Both the minimum and maximum calculated Young's moduli for the T-crystal were higher than those of any other crystal studied, confirming its superior rigidity, as observed experimentally. This enhanced stiffness is attributed to the more efficient steric packing within the T-crystal lattice. The spatial anisotropy of mechanical properties, including Young's modulus and shear modulus (Table S3 and Figs. S16–S18 in the supplementary information), exhibited a distinct butterfly-like [45] distribution with respect to crystallographic orientation. The anisotropy of the shear modulus components (e.g., c_{44}, c_{55}, and c_{66}) is particularly crucial, as it dominates the material's shear flexibility and bending behavior [18, 40, 46]. This structurally determined mechanical anisotropy, when coupled with the crystals' inherent non-centrosymmetric nature, provides the basis for understanding the anisotropic piezoelectric response observed in these materials.

3.3 Fabrication and testing of the piezoelectric bioelectronics

In addition to examining their favorable mechanical properties, we investigated the piezoelectric behavior of T crystals, as this functional characteristic is crucial for mechanical energy harvesting and sensing in flexible electronics. The non-centrosymmetric structure of biological amino acid molecular crystals gives rise to spontaneous polarization within the crystal, which is a fundamental prerequisite for piezoelectricity [47, 48]. The piezoelectric effect, as an important class of electromechanical phenomena, originates microscopically from the asymmetric charge distribution resulting from the non-centrosymmetric crystal structure. Under mechanical stress, the relative displacement of positive and negative charge centers induces macroscopic electrode formation, thereby enabling direct conversion of mechanical energy into electrical energy.

The generation of the piezoelectric effect relies on non-centrosymmetric structures and the ordered arrangement of molecular polarization. Although both T and Y crystals belong to the $P2_12_12_1$ non-centrosymmetric space group, the 3D hydrogen-bonding network in the T crystal not only enhances packing density but also, through electrostatic interactions (a zipper-like interlocking of NH_3^+ and COO^- groups), constrains the molecular alignment. This results in a more cooperative polarization orientation within the crystal. Conversely, the presence of C−H···π interactions in Y crystals disrupts the continuity of the hydrogen-bonding network, resulting in a lower molecular polarization orientation order compared to T. Consequently, T crystals exhibit a higher d_{33} value (2.86 pm/V) [17, 49, 50] (Fig. 3a; Figs. S19 and S20 in the supplementary information). Although this d_{33} value is not outstanding compared to inorganic ceramics like BTO, it is comparable to that of other bio-organic crystals (e.g., Cbz-pentafluoro-Phe, approximately 2.0 pm/V) [51] (Table S4 in the supplementary information). The core advantage of T-crystal in this study lies not in pursuing extreme piezoelectric output, but in its unique combination

Table 1 Young's modulus statistics of amino acid crystals with different side chains

Method	Type	Young's modulus (GPa)				
		F	Y	DOPA	S	T
Calculation	Min.	16.2	7.8	18.6	16.9	26.5
	Max.	41.3	45.2	65.3	49.6	79.7
Experiment	AFM	10.4±0.1	41.3±0.4	43.7±0.7	35.3±0.1	83.7±0.5
	Nanoindenter	–	27.4±1.0	23.1±1.5	18.9±1.1	30.6±1.0

AFM: atomic force microscopy

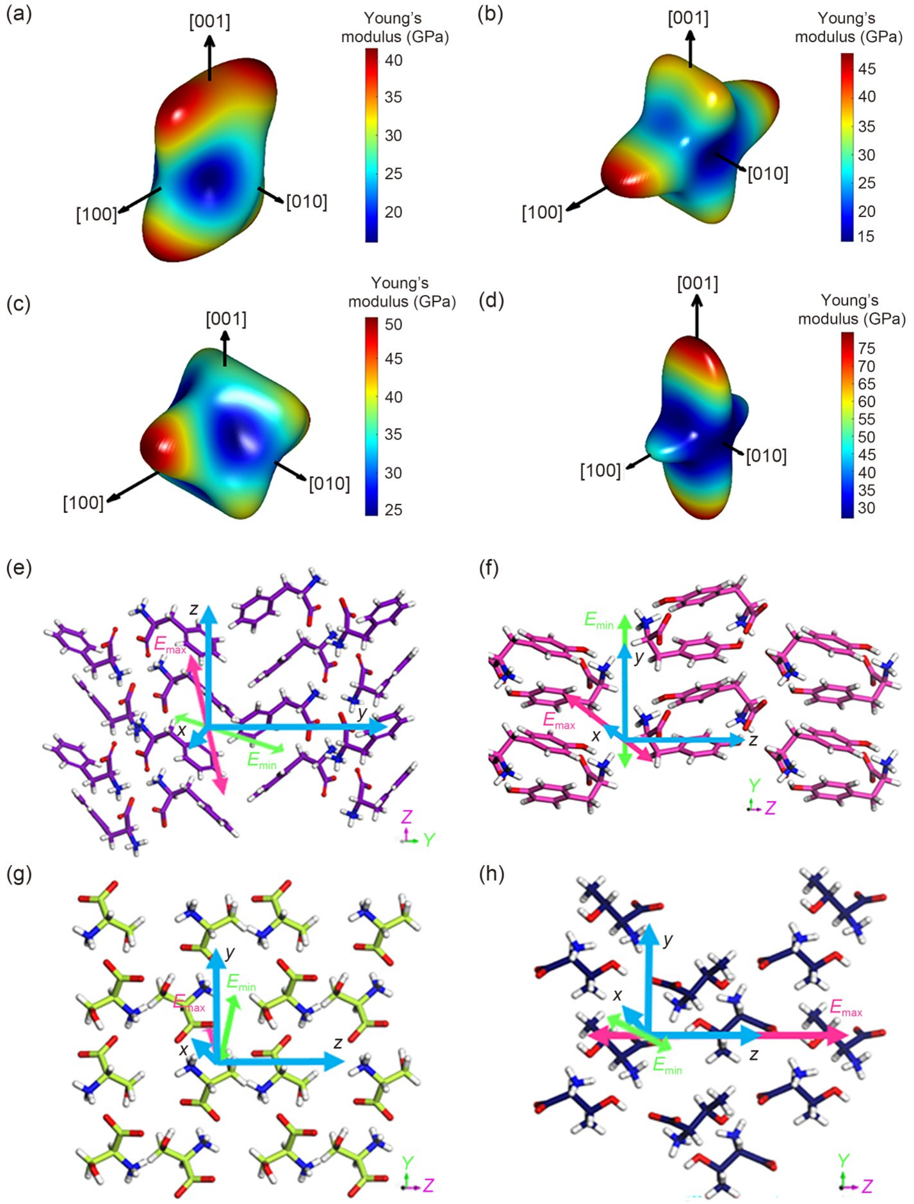

Fig. 2 Computed 3D rendering of the Young's moduli of F (a), Y (b), S (c), and T (d) crystals. The $E_{\max}$ (rose line) and $E_{\min}$ (green line) directions are signified in F (e), Y (f), S (g), and T (h) crystals

of ceramic-like high mechanical stiffness (approximately 80 GPa), biocompatibility derived from natural metabolites, and complete biodegradability. This characteristic combination directly addresses the core challenge faced by traditional piezoelectric materials in implantable applications: achieving both high performance and biological safety simultaneously. The DFT calculations revealed an increasing trend in molecular dipole moments: Y (2.16 D)<F (2.21 D)<DOPA (2.22 D)<S (2.27 D)<T (2.33 D) (1 D=3.335 64×10^{-30} C·m; Fig. S21 in the supplementary information). Crucially, unlike the loose packing in F or the layered structure in S, the dense 3D hydrogen-bond network in the T crystals synergistically aligns these high dipoles per unit volume, maximizing the macroscopic piezoelectric response without requiring complex tensor analysis.

Furthermore, in the non-centrosymmetric structures F ($P2_1$ space group) and S (P_n space group), the layered molecular stacking (S) or low packing density (F) further diminishes polarization efficiency, resulting in weaker piezoelectric responses than in the T crystal. Consistent results were obtained from crystal films using a quasi-static d_{33} piezometer (Fig. S22 in the supplementary information), supporting PFM measurements. As illustrated in Fig. 3b, a flexible sensor was constructed by sandwiching piezoelectric T crystals between two PAN electrode layers, followed by encapsulation with two PLA layers to form a five-layered

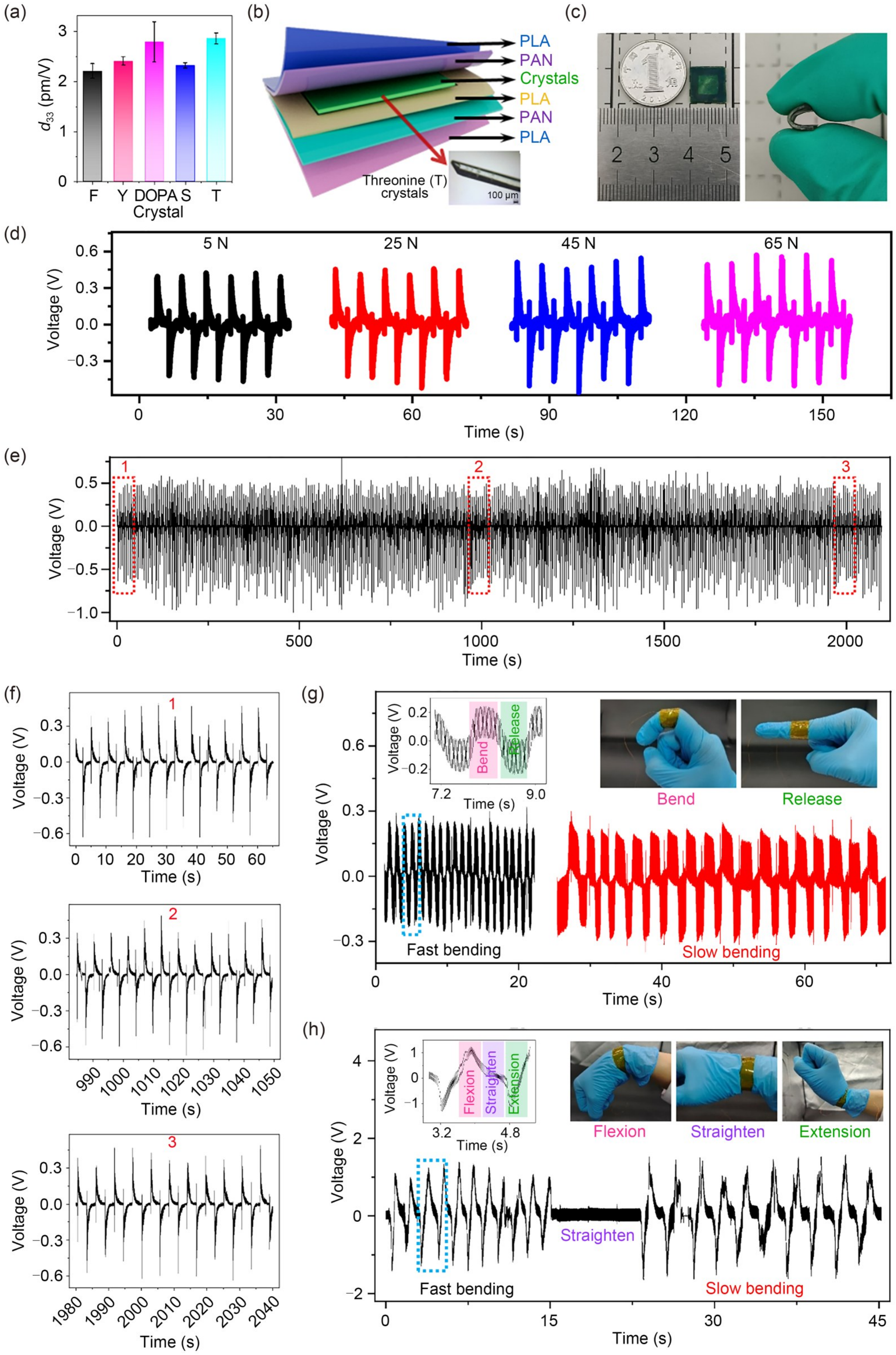

Fig. 3 Fabrication and characterization of the piezoelectric bioelectronics comprising T crystals. (a) Measured oscillating amplitude as a function of the applied AC signals, where the slope represents the piezoelectric constant d_{33}. Data are expressed as mean±standard deviation (N=3 independent experiments). (b) Schematic diagram showing the configuration of the piezoelectric device. (c) Size (left) and bending flexibility (right) of the fabricated prototype. (d) Open-circuit voltages of the fabricated sensor under different forces. (e) Output voltage of the fabricated sensor under 25 N compression. (f) Illustration of the magnification of the collected signal, representing its reproducibility. (g) Open-circuit voltages of the fabricated sensor fixed to a human finger during fast and slow bending. The insets depict a schematic of the sensor's movement on the finger. (h) Open-circuit voltage of a flexible sensor fixed on a human wrist during bending. The insets show the movements of the flexible sensor on the wrist

structure. The resulting sensor (10 mm×10 mm×1 mm) demonstrated good bending flexibility (Fig. 3c). Cross-sectional SEM images confirmed layer integrity: the PLA substrate was smooth, and the PAN coating formed a uniform, adherent conductive layer (Fig. S23 in the supplementary information). The combined PLA-PAN substrate exhibited notable flexibility, tensile and tear resistance, and no delamination or cracking, thereby facilitating robust sensor fabrication (Fig. S24 in the supplementary information).

The T-crystal-based sensor displayed a linear response over a 13-fold range from 5 to 65 N (Fig. 3d). This linear behavior was also observed in the other single crystals examined in this study (Fig. S25 in the supplementary information), indicating that natural amino acid crystals and their derivatives are suitable piezoelectric materials for such sensors. Control sensors without crystal layers produced negligible piezoelectric output (Fig. S26 in the supplementary information), confirming that the voltage signal originated from the piezoelectric core. Long-term stability and reproducibility were assessed under cyclic square-wave loading at 25 N. As shown in Figs. 3e and 3f, the open-circuit voltage signal returned to baseline within 5 s and maintained consistent amplitude and exponential decay over approximately 2000 s, with reproducible behavior throughout the testing period.

To further quantify the device's output capability, the short-circuit current was measured as approximately 120 nA under a 25-N load (Fig. S27 in the supplementary information), corresponding to an instantaneous power density of 0.192 μW/cm^2. Furthermore, the long-term reliability was verified by re-testing the sensor after 14 d of storage (Fig. S28 in the supplementary information). The device maintained a consistent output signal without noticeable degradation, highlighting its excellent environmental stability for practical usage. The sensor was also used to monitor finger and wrist motion (Figs. 3g and 3h), yielding periodic output signals the frequency of which varied with the movement. These results demonstrate the potential of the sensor for tracking biomechanical motion across different amplitudes and frequencies, supporting possible in vivo applications, and confirming the device's structural integrity, robustness, and reproducibility.

Although the biodegradable PLA substrate and PAN conductive layer provide good biocompatibility, the high electrical resistance of the amino acid crystal limited the open-circuit voltage output of the flexible sensor. To enhance electrical performance, the PLA substrate was replaced with a more rigid silicon wafer, and the PAN layer was substituted with metallic silver (Ag). This design leverages the dimensional stability of silicon and the high conductivity of silver to effectively mitigate resistive losses in the system. The optimized device achieved a substantially higher open-circuit voltage output of 1–2 V (Fig. S29 in the supplementary information).

3.4 In vivo application of the piezoelectric bioelectronics

Having validated the piezoelectric response of the T crystals, we further evaluated the biocompatibility and performance of the fabricated flexible sensor for potential implantable applications. The cytotoxicity of the sensor was assessed in vitro using human breast cancer cells (MDA-MB-231). Cells were cultured with varying concentrations of the sensor extract, and viability was assessed using a cell counting kit-8 (CCK-8) assay. After 24 h (Fig. S30 in the supplementary information) or 48 h (Fig. 4a) of co-incubation, cell viability remained approximately 99%, showing no significant difference from the blank control group, indicating very low cytotoxicity. This finding was further supported by morphological examination of the cytoskeletal network (Fig. 4b; Fig. S31 in the supplementary information) and direct live/dead fluorescence staining (Fig. 4c; Fig. S32 in the supplementary information). The cytoskeleton (red) and nuclei (blue) appeared similar to those of the control group, and the majority of cells stained live with Calcein-AM (green) over 24–48 h. Collectively, these results confirm the remarkably low cytotoxicity of the prepared sensor.

Given its favorable biocompatibility in vitro, the flexible sensor was implanted subcutaneously in mice to evaluate in vivo biocompatibility and biodegradation. The tissue surrounding the implant was harvested on Days 5, 7, 12, 28, 35, and 52 post-operation for hematoxylin and eosin (H&E) staining and Masson's trichrome staining, and blood samples were collected for analysis. As shown in Fig. 4d, the surrounding tissue maintained its layered architecture with minimal disruption from the implant. Histological analysis [52–54] (Figs. S33–S37 in the supplementary information) revealed initial immune cell infiltration between Days 5 and 7, with the immune response peaking around Days 12–28, coinciding with the active phase of biodegradation. By Day 35, the immune response had returned to normal levels, and tissue healing was complete, consistent with macroscopic observations (Fig. S33a in the supplementary information). Quantification of immune cell count and optical density indicated only mild inflammation by Day 28, with toxicity comparable to that of the sham control, and a return to baseline by Day 35 (Figs. 4e and 4f), consistent with reported flexible devices. Meanwhile, statistical analysis of fibrous capsule thickness revealed that the sensor induced an extremely mild foreign body response compared to the control group (Fig. 4g). Furthermore, hematological analysis showed no significant differences from the control group, with white blood cell, red blood cell, hemoglobin, and platelet counts all within normal ranges (Figs. S33b–S33e in the supplementary information). Under physiological conditions in simulated body fluid (SBF) at 37 °C, the sensor's mass decreased to below 50% after 6 weeks (Fig. S38 in the

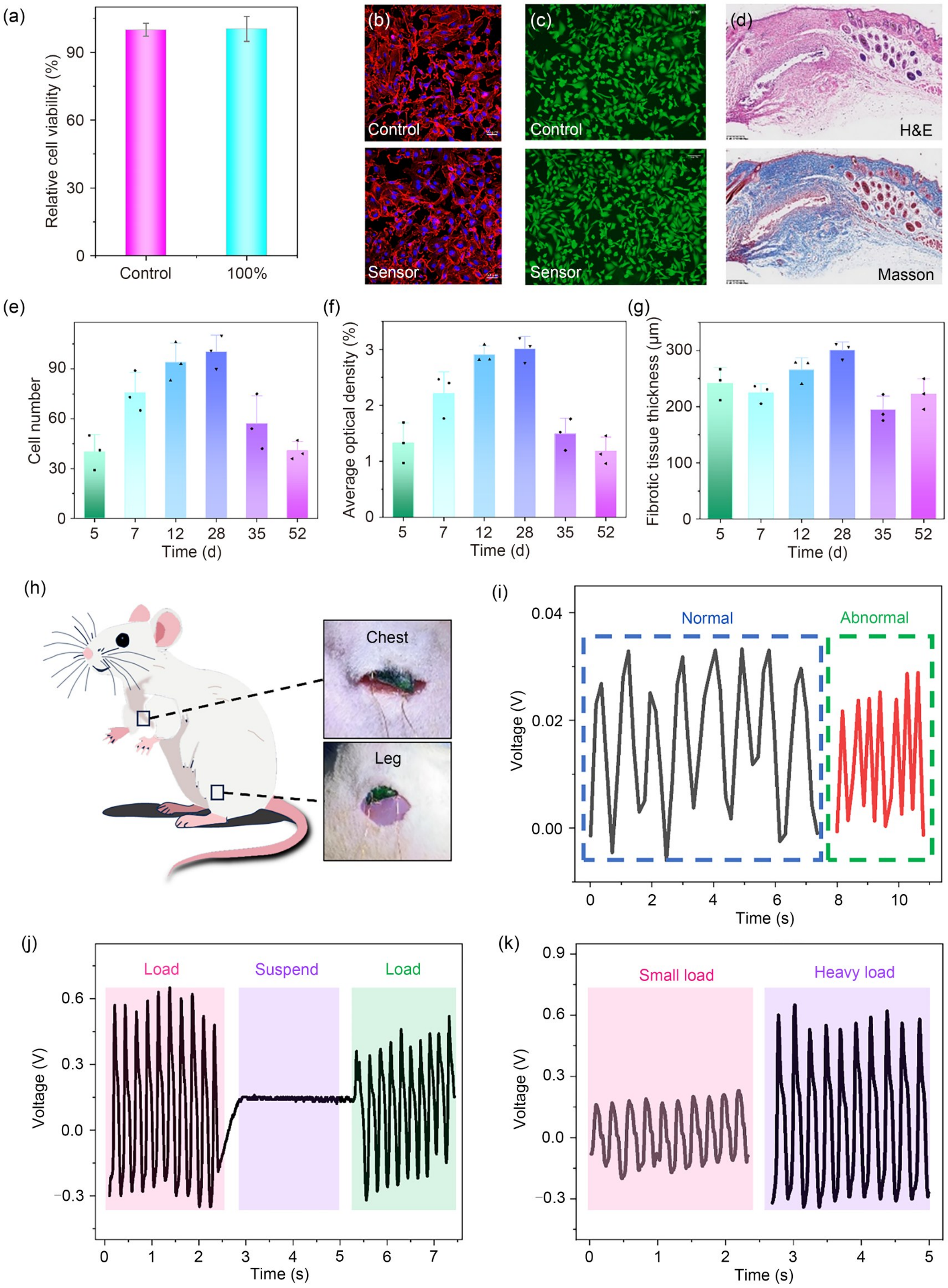

Fig. 4 In vivo detection of T-crystal-based piezoelectric bioelectronics. (a) Cell viability of MDA-MB-231 cells co-cultured with a flexible sensor for 48 h. The control group was normalized to 100% as the baseline reference. (b) Fluorescent images of the MDA-MB-231 cells cultured with the flexible sensor. Cytoskeleton and nuclei were stained with phalloidin (red) and DAPI (blue) after 48 h of incubation. Scale bars: 50 μm. (c) Live (green)/dead (red) double staining of MDA-MB-231 cells with the sensor extraction for 48 h. Scale bar: 100 μm. (d) Typical histological images stained with H&E (top) and Masson's trichrome (bottom) at 28 d after subcutaneous implantation of the PLA-PAN membrane. Scale bars: 200 μm. Statistics of immune cell number (e) and mean optical density (f) from image (d). The cell number in the proliferation assay was counted within a 200 μm×200 μm microscope field. (g) Statistics of Masson staining for collagen fiber thickness. (h) Illustrations of subcutaneously implanted sensors in the chest and legs of Sprague–Dawley rats. (i) Output open-circuit voltage signal of a flexible sensor implanted in the chest due to respiration. Output open-circuit voltage of a flexible sensor implanted in the leg under periodical gentle stretching upon periodic pressing load (j) and variable amplitudes of the loading (k). Data in (a, e–g) are expressed as mean±standard deviation (*N*=3 independent experiments)

supplementary information). These data collectively demonstrate good in vivo biocompatibility and minimal systemic toxicity.

As a transient implantable bioelectronic device, the synchrony between its functional lifespan and degradation curve is critical. The PLA encapsulation layer in this design is engineered to maintain structural integrity for approximately 35 d, which aligns with tissue-healing cycles. During this period, the T-crystal core remains effectively shielded from bodily fluid erosion, ensuring stable and reliable piezoelectric signal output for diagnostic monitoring. As demonstrated by in vitro degradation experiments (Fig. S38 in the supplementary information), significant mass loss commences beyond this window. Once the PLA barrier is compromised, the water-soluble T-crystal rapidly dissolves, causing a steep decline in sensor functionality and eventual failure. Based on our degradation data (mass loss of almost 50% after 6 weeks) and histological observations (immune response peaking between 12 and 28 d), we infer that significant performance degradation may commence within 3–4 weeks post-implantation. Therefore, we estimate that its effective functional lifespan falls within this timeframe. This behavior aligns with application requirements, enabling the device to perform its function during the monitoring period before degrading safely, thereby achieving the ultimate goal of “no need for secondary surgery for removal.”

Based on these findings, the T-crystal-based flexible sensor was subcutaneously implanted in the chest and left hind leg regions of Sprague–Dawley rats (Fig. 4h). Two insulated wires were used to transmit real-time electrical signals during respiration. Under stable physiological conditions, the sensor clearly recorded the rat’s regular respiratory rhythm, producing voltage signals with stable periodic fluctuations (left panel of Fig. 4i). Notably, when the rat was subjected to external stimuli, such as elevated ambient temperature or drug injection, its respiratory pattern changed to a rapid, shallow rhythm. The sensor sensitively captured this dynamic change, with the output voltage signal showing a distinct increase in fluctuation frequency and waveform density (right panel of Fig. 4i). These results confirm the high sensitivity and real-time response of the sensor for monitoring physiological signals in vivo, and suggest its potential for tracking dynamic changes during emotional or stress states.

Similarly, when implanted in the hind leg, the sensor responded to passive mechanical stretching. Upon stretching and releasing the leg, a significant, reproducible voltage signal was generated. The signal quickly returned to baseline when stretching was paused and recovered promptly when stretching resumed (Fig. 4j), demonstrating high sensitivity to the onset and cessation of mechanical stimuli. Under different stretching loads (Fig. 4k), a small load produced a low-amplitude voltage fluctuation (approximately 0.3 V), whereas a larger load resulted in a substantially higher amplitude (approximately 0.9 V), indicating the sensor’s ability to distinguish between different mechanical stimulus intensities. The larger signal amplitude observed in the leg compared with the chest is consistent with the greater deformation during limb motion. These in vivo results validate the sensor’s specificity and intensity discrimination in dynamic mechanical monitoring, supporting its potential for the real-time tracking of limb movement and localized mechanical loading.

In summary, these findings demonstrate the successful fabrication of a flexible sensor based on amino acid crystals. The sensor exhibits good biocompatibility, controlled biodegradation dynamics, low systemic and hematological toxicity, and reliable performance for in vivo monitoring of physiological and mechanical signals, rendering it suitable for implantable motion-sensing applications. Even with the self-induced, non-ideal alignment of the crystals within the current sensor matrix (lacking active external optimization), the intrinsic mechanical anisotropy and high stiffness of the T crystals ensure effective stress transmission, enabling robust performance. This confirms the material’s inherent robustness for facile device fabrication, while the anisotropy data provide a theoretical roadmap for future performance enhancement via deliberate directional alignment.

4 Conclusions

This study investigated the intrinsic electromechanical coupling properties and potential applications of natural amino acid non-centrosymmetric crystals, particularly the influence of side chains on crystal packing, mechanical properties, and piezoelectric responses. Through a combination of experimental and computational analysis, we determined that the polarity (hydroxyl groups) and volume of the side chains dominate the crystal packing mode by modulating the non-covalent interaction network. In particular, the 3D hydrogen-bond network in T crystals (each molecule interacting with seven neighbors) conferred an ultra-high Young’s modulus up to approximately 80 GPa, providing structural support for bioelectronics engineering. The degree of ordered molecular polarization within the non-centrosymmetric structure was critical to the piezoelectric response. T crystals exhibited a d_{33} value of 2.86 pm/V, demonstrating tremendous electromechanical conversion capability. Therefore, flexible piezoelectric bioelectronics comprising T crystals exhibited a linear response, allowing them to be employed for in vitro and in vivo biocompatibility (approximately 99% cell viability, complete tissue healing within 35 d) and for the real-time monitoring of physiological signals (respiration, limb movement). The paradigm established in this work provides alternative insights for the design of next-generation biosafe piezoelectric entities, along with the intrinsic biodegradable nature, which lays the groundwork for the clinical translation of implantable bioelectronics.

Supplementary Information The online version contains supplementary material available at https://doi.org/10.1631/bdm.2600041.

Acknowledgements The work was supported by the "Pioneer" and "Leading Goose" R&D Program of Zhejiang Province (No. 2025C04010), the National Key R&D Program of China (No. 2025YFE0125200), the National Natural Science Foundation of China (Nos. 52175551 and 21673293), the Fundamental Research Funds for the Central Universities (No. 226-2025-00194), and the Key Research and Development Program of Zhejiang Province (No. 2025C01003). The authors thank all laboratory members for their insightful discussions and valuable feedback throughout the project.

Author contributions HX and KT conceived and designed the work. ZFQ, RQL, HYJ, and XYM conducted the crystal growth and further characterizations. ZFQ, LJG, and ZXL conducted the Young's modulus measurement. JHZ, YCW, JQW, SAMT, and DQM provided language editing. ZFQ coordinated all the work, analyzed the results, and wrote and edited the manuscript with input from all authors. All authors gave permission for the final version of the publication.

Declarations

Conflict of interest KT is an academic editor of *Bio-Design and Manufacturing* and was not involved in the editorial review or the decision to publish this article. The authors declare that they have no conflict of interest.

Ethical approval All experimental procedures were performed in accordance with relevant guidelines and regulations. The study was approved by the Animal Care and Use Committee of Zhejiang University (Approval No. ZJU20241081; approved on 2025-04-15; valid until 2029-01-13). Written informed consent (both for participation and publication) was obtained from the volunteer who participated in the human body motion monitoring experiments.

Data availability The datasets generated and/or analyzed during this study are available from the corresponding authors upon reasonable request.

Use of generative AI tools No generative AI tools were used during the preparation of this manuscript.

References

1. Cheng YQ, Wang TJ, Zhu HQ et al (2025) Molecular engineering of amino acid crystals with enhanced piezoelectric performance for biodegradable sensors. *Angew Chem Int Ed* 64(15): e202500334. https://doi.org/10.1002/anie.202500334
2. Cheng YQ, Xu J, Li L et al (2023) Boosting the piezoelectric sensitivity of amino acid crystals by mechanical annealing for the engineering of fully degradable force sensors. *Adv Sci* 10(11):2207269. https://doi.org/10.1002/advs.202207269
3. Jiang YW, Zhang ZT, Wang YX et al (2022) Topological supramolecular network enabled high-conductivity, stretchable organic bioelectronics. *Science* 375(6587):1411–1417. https://doi.org/10.1126/science.abj7564
4. Wu HR, Lyu H, Jiang HB et al (2025) Bioinspired supramolecular fibrillization enables stretchable and biodegradable piezoelectric bioelectronics. *Sci Adv* 11(25):eadu6759. https://doi.org/10.1126/sciadv.adu6759
5. Zhang ZM, Wang ZQ, Li XM et al (2025) Design and manufacturing of piezoelectric biomaterials for bioelectronics and biomedical applications. *Chem Rev* 125(20):9875–9929. https://doi.org/10.1021/acs.chemrev.5c00399
6. Tao K, Hu W, Xue B et al (2019) Bioinspired stable and photoluminescent assemblies for power generation. *Adv Mater* 31(12): e1807481. https://doi.org/10.1002/adma.201807481
7. Gao LJ, Liu ZX, Dikovsky D et al (2024) Innovation leading development: a glimpse into three-dimensional bioprinting in Israel. *Bio-Des Manuf* 7(3):358–382. https://doi.org/10.1007/s42242-024-00275-5
8. Wang Z, Liu ZR, Zhao GR et al (2022) Stretchable unsymmetrical piezoelectric $BaTiO_3$ composite hydrogel for triboelectric nanogenerators and multimodal sensors. *ACS Nano* 16(1):1661–1670. https://doi.org/10.1021/acsnano.1c10678
9. Pratihar S, Chandran AM, Bhat AR et al (2024) Piezoelectric nanogenerators based on poly(vinylidene fluoride) doped with high entropy oxide nanoparticles for sensitive pressure sensors. *ACS Appl Nano Mater* 7(17):20553–20568. https://doi.org/10.1021/acsanm.4c03569
10. Surmenev RA, Chernozem RV, Pariy IO et al (2021) A review on piezo- and pyroelectric responses of flexible nano- and micropatterned polymer surfaces for biomedical sensing and energy harvesting applications. *Nano Energy* 79:105442. https://doi.org/10.1016/j.nanoen.2020.105442
11. Vijayakanth T, Liptrot DJ, Gazit E et al (2022) Recent advances in organic and organic–inorganic hybrid materials for piezoelectric mechanical energy harvesting. *Adv Funct Mater* 32(17):2109492. https://doi.org/10.1002/adfm.202109492
12. Zhang Y, Li Q, Wu HR et al (2023) Racemic amino acid assembly enables supramolecular β-sheet transition with property modulations. *ACS Nano* 17(3):2737–2744. https://doi.org/10.1021/acsnano.2c11006
13. Ji W, Xue B, Arnon ZA et al (2019) Rigid tightly packed amino acid crystals as functional supramolecular materials. *ACS Nano* 13(12):14477–14485. https://doi.org/10.1021/acsnano.9b08217
14. Yuan H, Xue B, Yang DY et al (2023) Rational design of biological crystals with enhanced physical properties by hydrogen bonding interactions. *Research* 6:0046. https://doi.org/10.34133/research.0046
15. Owczarek M, Hujsak KA, Ferris DP et al (2016) Flexible ferroelectric organic crystals. *Nat Commun* 7:13108. https://doi.org/10.1038/ncomms13108
16. Bhunia S, Karan SK, Chowdhury R et al (2024) Mechanically flexible piezoelectric organic single crystals for electrical energy harvesting. *Chem* 10(6):1741–1754. https://doi.org/10.1016/j.chempr.2024.01.019
17. Bhunia S, Chandel S, Karan SK et al (2021) Autonomous self-repair in piezoelectric molecular crystals. *Science* 373(6552): 321–327. https://doi.org/10.1126/science.abg3886
18. Guerin S, Stapleton A, Chovan D et al (2018) Control of piezoelectricity in amino acids by supramolecular packing. *Nat Mater* 17(2):180–186.

https://doi.org/10.1038/nmat5045

19. Ji W, Xue B, Yin YY et al (2022) Modulating the electromechanical response of bio-inspired amino acid-based architectures through supramolecular co-assembly. *J Am Chem Soc* 144(40): 18375–18386. https://doi.org/10.1021/jacs.2c06321
20. Bera S, Guerin S, Yuan H et al (2021) Molecular engineering of piezoelectricity in collagen-mimicking peptide assemblies. *Nat Commun* 12(1):2634. https://doi.org/10.1038/s41467-021-22895-6
21. Kresse G, Furthmüller J (1996) Efficiency of ab-initio total energy calculations for metals and semiconductors using a plane-wave basis set. *Comput Mater Sci* 6(1):15–50. https://doi.org/10.1016/0927-0256(96)00008-0
22. Kresse G, Furthmüller J (1996) Efficient iterative schemes for *ab initio* total-energy calculations using a plane-wave basis set. *Phys Rev B* 54(16):11169–11186. https://doi.org/10.1103/physrevb.54.11169
23. Perdew JP, Burke K, Ernzerhof M (1996) Generalized gradient approximation made simple. *Phys Rev Lett* 77(18):3865–3868. https://doi.org/10.1103/PhysRevLett.77.3865
24. Kresse G, Joubert D (1999) From ultrasoft pseudopotentials to the projector augmented-wave method. *Phys Rev B* 59(3):1758–1775. https://doi.org/10.1103/physrevb.59.1758
25. Blöchl PE (1994) Projector augmented-wave method. *Phys Rev B* 50(24):17953–17979. https://doi.org/10.1103/physrevb.50.17953
26. Monkhorst HJ, Pack JD (1976) Special points for Brillouin-zone integrations. *Phys Rev B* 13(12):5188–5192. https://doi.org/10.1103/physrevb.13.5188
27. Grimme S, Antony J, Ehrlich S et al (2010) A consistent and accurate *ab initio* parametrization of density functional dispersion correction (DFT-D) for the 94 elements H-Pu. *J Chem Phys* 132(15):154104. https://doi.org/10.1063/1.3382344
28. Grimme S, Ehrlich S, Goerigk L (2011) Effect of the damping function in dispersion corrected density functional theory. *J Comput Chem* 32(7):1456–1465. https://doi.org/10.1002/jcc.21759
29. Marmier A, Lethbridge ZAD, Walton RI et al (2010) ElAM: a computer program for the analysis and representation of anisotropic elastic properties. *Comput Phys Commun* 181(12):2102–2115. https://doi.org/10.1016/j.cpc.2010.08.033
30. Gaillac R, Pullumbi P, Coudert FX (2016) ELATE: an open-source online application for analysis and visualization of elastic tensors. *J Phys Condens Matter* 28(27):275201. https://doi.org/10.1088/0953-8984/28/27/275201
31. Wang YH, Liu SJ, Li LL et al (2023) Manipulating the piezoelectric response of amino acid-based assemblies by supramolecular engineering. *J Am Chem Soc* 145(28):15331–15342. https://doi.org/10.1021/jacs.3c02993
32. Hu J, Liu SJ, Huo YH et al (2025) Piezoelectric vitamin-based self-assemblies for energy generation. *Adv Mater* 37(9):e2417409. https://doi.org/10.1002/adma.202417409
33. Zardecki C, Dutta S, Goodsell DS et al (2022) PDB-101: educational resources supporting molecular explorations through biology and medicine. *Protein Sci* 31(1):129–140. https://doi.org/10.1002/pro.4200
34. Prazyan TL, Zhuravlev YN, Golovko OV et al (2019) DFT-study of pressure-induced phase transition in *L*-threonine. *J Mol Struct* 1196:271–279. https://doi.org/10.1016/j.molstruc.2019.06.077
35. Desiraju G, Steiner T (2001) The Weak Hydrogen Bond: in Structural Chemistry and Biology. Oxford University Press Inc., USA. https://doi.org/10.1093/acprof:oso/9780198509707.001.0001
36. Karothu DP, Dushaq G, Ahmed E et al (2021) Mechanically robust amino acid crystals as fiber-optic transducers and wide bandpass filters for optical communication in the near-infrared. *Nat Commun* 12(1):1326. https://doi.org/10.1038/s41467-021-21324-y
37. Sögütoglu LC, Lutz M, Meekes H et al (2017) Polymorphism and modulation of para-substituted *L*-phenylalanine. *Cryst Growth Des* 17(12):6231–6238. https://doi.org/10.1021/acs.cgd.7b00747
38. Mossou E, Teixeira SCM, Mitchell EP et al (2014) The self-assembling zwitterionic form of *L*-phenylalanine at neutral pH. *Acta Crystallogr C Struct Chem* 70(3):326–331. https://doi.org/10.1107/S2053229614002563
39. Yuan CQ, Ji W, Xing RR et al (2019) Hierarchically oriented organization in supramolecular peptide crystals. *Nat Rev Chem* 3(10):567–588. https://doi.org/10.1038/s41570-019-0129-8
40. Matveychuk YV, Bartashevich EV, Tsirelson VG (2018) How the H-bond layout determines mechanical properties of crystalline amino acid hydrogen maleates. *Cryst Growth Des* 18(6): 3366–3375. https://doi.org/10.1021/acs.cgd.8b00067
41. Mishra MK, Ramamurty U, Desiraju GR (2016) Mechanical property design of molecular solids. *Curr Opin Solid State Mater Sci* 20(6):361–370. https://doi.org/10.1016/j.cossms.2016.05.011
42. Zolotarev PN, Moret M, Rizzato S et al (2016) Searching new crystalline substrates for OMBE: topological and energetic aspects of cleavable organic crystals. *Cryst Growth Des* 16(3):1572–1582. https://doi.org/10.1021/acs.cgd.5b01695
43. Wang CG, Sun CC (2020) The landscape of mechanical properties of molecular crystals. *CrystEngComm* 22(7):1149–1153. https://doi.org/10.1039/C9CE01874C
44. Azuri I, Meirzadeh E, Ehre D et al (2015) Unusually large Young's moduli of amino acid molecular crystals. *Angew Chem Int Ed* 54(46):13566–13570. https://doi.org/10.1002/anie.201505813
45. Knowles TPJ, Mezzenga R (2016) Amyloid fibrils as building blocks for natural and artificial functional materials. *Adv Mater* 28(31):6546–6561. https://doi.org/10.1002/adma.201505961
46. Dagdeviren C, Su YW, Joe P et al (2014) Conformable amplified lead zirconate titanate sensors with enhanced piezoelectric response for cutaneous pressure monitoring. *Nat Commun* 5: 4496. https://doi.org/10.1038/ncomms5496
47. Yuan H, Han PP, Tao K et al (2019) Piezoelectric peptide and metabolite materials. *Research* 2019:9025939. https://doi.org/10.34133/2019/9025939
48. Chen BJ, Feng ZM, Yao FZ et al (2025) Flexible piezoelectrics: integration of sensing, actuating and energy harvesting. *npj Flex Electron* 9:58. https://doi.org/10.1038/s41528-025-00432-5
49. Zhang HY, Chen XG, Tang YY et al (2021) PFM (piezoresponse force microscopy)-aided design for molecular ferroelectrics. *Chem Soc Rev* 50(14):8248–8278. https://doi.org/10.1039/c9cs00504h
50. Buragohain P, Lu HD, Richter C et al (2022) Quantification of the electromechanical measurements by piezoresponse force

microscopy. *Adv Mater* 34(47):2206237. https://doi.org/10.1002/adma.202206237

51. Hu T, Lee JP, Huang PW et al (2025) Promoting piezoelectricity in amino acids by fluorination. *Adv Mater* 37(3):2413049. https://doi.org/10.1002/adma.202413049
52. Wang WH, Wu FY, Wu Z et al (2025) The XIAP inhibitor AZD5582 improves the treatment effect of microwave ablation on hepatocellular carcinoma. *Front Immunol* 16:1482954. https://doi.org/10.3389/fimmu.2025.1482954
53. Fernandes DP, Pimentel MML, Dos Santos FA et al (2018) Hematological and biochemical profile of BALB/c nude and C57BL/6 SCID female mice after ovarian xenograft. *An Acad Bras Ciênc* 90(4):3941–3948. https://doi.org/10.1590/0001-3765201820180586
54. Santos EW, de Oliveira DC, Hastreiter A et al (2016) Hematological and biochemical reference values for C57BL/6, Swiss Webster and BALB/c mice. *Braz J Vet Res Anim Sci* 53(2):138. https://doi.org/10.11606/issn.1678-4456.v53i2p138-145